

www.acsaem.org Article

# Fluorobenzene-Diluted Localized Highly Concentrated Electrolyte for Enhanced Electrochemical Performance of Li-O<sub>2</sub> Battery

Syed Shoaib Hassan Zaidi, Justin T. Douglas, and Xianglin Li\*



Cite This: ACS Appl. Energy Mater. 2024, 7, 8610-8621



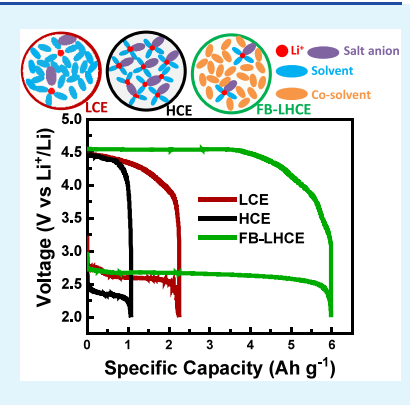
**ACCESS** I

III Metrics & More

Article Recommendations

s Supporting Information

ABSTRACT: Highly concentrated electrolytes (HCEs), owing to their high thermal and chemical stability, wider electrochemical stability windows (ESWs), and enhanced stability with Li metal anode, have been under the spotlight as a potential electrolyte candidate for developing Li-O<sub>2</sub> batteries. Nonetheless, their high viscosity, poor wettability, and high cost pose great challenges in achieving the desired results. In this study, we designed an HCE diluted with a low-polarity hydrocarbon cosolvent, fluorobenzene, and investigated its electrochemical performance in a Li-O<sub>2</sub> battery. Raman spectroscopy analysis and self-diffusivity coefficients of electrolyte components determined by nuclear magnetic resonance (NMR) technique have confirmed that the fluorobenzene-based localized highly concentrated electrolyte (FB-LHCE) conserved the unique solvation structure of contact ion pairs and cation—anion aggregates formed in HCE. Incorporating fluorobenzene into HCE improved the self-diffusivity of electrolyte components by over a magnitude, lowered the viscosity by over 40 times, and increased the ionic conductivity 5-fold. Furthermore, FB-



LHCE drastically improved the electrode wettability by yielding 3 and 5 orders of magnitude higher double-layer capacitances than those of low-concentration (LCE) and HCE, respectively. Additionally, when compared with LCE as the baseline, HCE and FB-LHCE have demonstrated wider anodic ESWs (>4.6 V). LillLi symmetric cell tests revealed significantly improved electrochemical stability of HCE and FB-LHCE with Li metal anode compared to LCE. HCE and FB-LHCE have yielded stable cycling for double the amount of time (1300 h) compared with LCE (650 h). FB-LHCE delivered the highest specific discharge capacity (6.0 Ah g<sup>-1</sup>) followed by LCE (2.25 Ah g<sup>-1</sup>) and HCE (1.07 Ah g<sup>-1</sup>) in Li–O<sub>2</sub> cells. Full-cell cycling stability tests have shown enhanced cycling stability with FB-LHCE (11 cycles) compared with those with LCE (2 cycles) and HCE (2 cycles).

**KEYWORDS:** Highly Concentrated Electrolyte, Fluorobenzene, Diluent, Stability, Li-O<sub>2</sub> Battery

## 1. INTRODUCTION

Owing to the extremely high theoretical energy density ( $\sim$ 3500 W h kg<sup>-1</sup>), a nonaqueous Li-O<sub>2</sub> battery has garnered enormous research interest over the past two decades and is considered a promising candidate for future energy storage applications. The high energy density of the Li-O<sub>2</sub> positive electrode stems from the fundamentally different discharge reaction than that of the Li-ion battery. In a Li-O<sub>2</sub> cell, molecular O<sub>2</sub> is reduced and combined with Li<sup>+</sup> to form an insoluble discharge product (typically Li<sub>2</sub>O<sub>2</sub>) on the surface of the porous electrode. During charging, Li<sub>2</sub>O<sub>2</sub> disintegrates to release Li<sup>+</sup> and the O<sub>2</sub> gas as reverse reaction products. The reaction mechanism is presented in eqs 1a-1c. The cathode electrode undergoes an oxygen reduction reaction (ORR) and an oxygen evolution reaction (OER) during the discharge and charge cycles, respectively.

anode:

$$2Li \leftrightarrow 2Li^{+} + 2e^{-} \tag{1a}$$

cathode:

$$2Li^{+} + 2e^{-} + O_{2} \leftrightarrow Li_{2}O_{2}$$
 (1b)

overall:

$$2\text{Li} + \text{O}_2 \leftrightarrow \text{Li}_2\text{O}_2$$
  $E^{\circ} = 2.96 \text{ V}$  (1c)

The reversibility and stable cycling of  $\text{Li-O}_2$  batteries are significantly affected by the choice of electrolyte incorporated. Conventional organic-solvent-based electrolytes do not withstand the corrosive environment of a battery and tend to deteriorate during battery cycling. The degradation of electrolytes primarily comes from two sources (i) parasitic reaction between nucleophilic superoxide  $(O_2^-)$  radical, which is generated during ORR, and (ii) continuous reaction with Li metal to form an unstable solid electrolyte interphase (SEI) layer.  $^{6-8}$  Electrolytes based on carbonates, ethers and amides were found to be unstable in  $\text{Li-O}_2$  battery in the previous studies.  $^{9-11}$  Dimethyl sulfoxide (DMSO) has been researched

Received: June 18, 2024
Revised: September 2, 2024
Accepted: September 3, 2024
Published: September 17, 2024





extensively and showcased superior performance in  $\text{Li-O}_2$  batteries owing to its high Guttmann donor number (DN = 29.8 kcal  $\text{mol}^{-1}$ ), enhanced  $\text{O}_2$  diffusivity, and ionic conductivity. Solvents exhibiting high DN tend to stabilize intermediate superoxide species and promote a solution mediated mechanism of discharge product formation, which results in higher capacity. However, the interfacial stability of DMSO with Li metal is questionable due to its inability to form a stable passivation layer, thereby continuously reacting with fresh Li metal. He conventional electrolytes, due to lower salt concentration, a fraction of solvent molecules coordinate with  $\text{Li}^+$  and exist as a solvent separated ion pair (SSIP), as illustrated in Figure 1a,b. Meanwhile, most of the

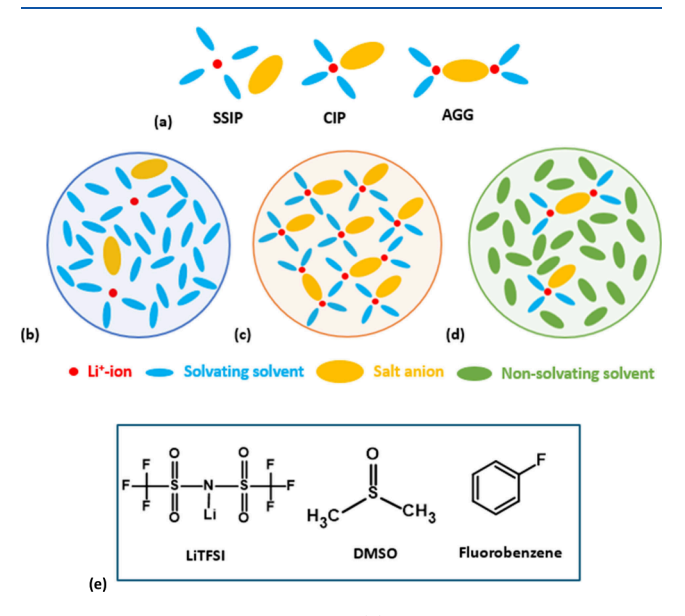


**Figure 1.** Schematic illustrations of (a) types of solvation structures. Components of (b) LCE, (c) HCE, and (d) FB-LHCE. (e) Chemical structures of LiTFSI, DMSO, and fluorobenzene.

solvent molecules remain uncoordinated in the solution. This renders them susceptible to attack by reactive superoxide radicals during the ORR. Furthermore, the SEI formed on the Li metal surface is mainly derived from the degradation of solvent molecules. The resulting SEI layer is not robust enough to sustain long battery cycling. <sup>16</sup>

High salt concentration electrolytes (HCEs) have been found to be an effective and promising approach in mitigating the decomposition of electrolytes during battery cycling. Furthermore, these electrolytes exhibit high thermal and chemical stability, wider electrochemical stability windows (ESWs), and lower volatility.<sup>17</sup> This is ascribed to the formation of a unique solvation structure in which all solvent molecules are coordinated with Li<sup>+</sup> unlike electrolytes with low salt concentrations. Additionally, due to the scarcity of uncoordinated solvent molecules, salt anions enter the solvation sheath and form a contact ion pair (CIP) and cation—anion aggregate (AGG) as shown in Figure 1a,c. The formation of a stable SEI layer on the Li metal anode is greatly affected by the solvation structure of the electrolyte. With higher salt concentrations, salt anions participate in SEI layer formation on the Li anode, thereby inhibiting the decomposition of solvent molecules.<sup>18</sup> High salt concentrations, however, bring other drawbacks, such as poor transport properties due to high viscosity, salt precipitation at lower

temperatures, poor wettability, and high cost. <sup>19</sup> To circumvent these challenges, non-solvating, and non-coordinating cosolvents are incorporated into HCEs which significantly improve the wettability and enhance the transport properties by lowering the viscosity. <sup>20</sup> The selected cosolvent must preserve the unique solvation structure of HCEs by avoiding coordination with Li<sup>+</sup> and must exist as free solvent molecules to form localized highly concentrated electrolytes (LHCEs), as illustrated in Figure 1d. Consequently, low-polarity solvents with low DN and low dielectric constants are utilized for this purpose.

Over the past few years, various forms of hydrofluoroethers (HFEs) employed as non-solvating diluents in HCEs have been investigated in Li batteries. <sup>21–23</sup> Zhao et al. incorporated 1,1,2,2-tetrafluoroethyl 2,2,3,3-tetrafluoropropyl ether (TTE) diluent into a highly concentrated tetraglyme electrolyte to form a binary mixture with improved wettability, enhanced ionic conductivity, and electrochemical stability. The cell with binary electrolyte yielded 600 h reversible discharge-charge cycles at a current density of 200 mA  $g^{-1}$  and with a fixed capacity of 1000 mAh  $g^{-1}$ . Kwak et al. employed 1*H*,1*H*,5*H*octafluoropentyl-1,1,2,2-tetrafluoroethyl ether (OTE) in tetraglyme-based HCE to obtain LHCE. OTE exhibits a higher boiling point than TTE (93 °C vs 133 °C), which renders it less volatile. OTE-based LHCE yielded 50 stable cycles compared with HCE (<15) and 1 M tetraglyme/salt (35) at a current density of 0.2 mA cm<sup>-2</sup> and with a limited areal capacity of 1.0 mAh  $\,\mathrm{cm}^{-2.25}$  In another study, the same group studied the performance of various fluorinated diluents with HCE in Li-O<sub>2</sub> batteries. OTE-based LHCE has demonstrated the highest chemical and electrochemical stability with Li metal. LillLi symmetric cell with LHCE-OTE has shown stable cycling for 500 h. Furthermore, the activation energy calculated for the OTE confirmed its stability in the presence of singlet oxygen. Watanabe and co-workers have significantly contributed toward understanding the impact of HCEs and LHCEs on battery stability in their various studies. 26-28

The area of LHCEs is relatively novel and less explored and requires special attention, especially in Li-O<sub>2</sub> battery systems. We designed a dimethyl sulfoxide (DMSO)-based HCE diluted with a low-polarity hydrocarbon cosolvent, fluorobenzene (FB), to form a localized highly concentrated electrolyte (FB-LHCE). Figure 1e shows the chemical structures of LiTFSI, DMSO, and FB. The performance of FB-LHCE in Li-O2 batteries is investigated for the first time. FB, as a cosolvent, has the advantage of cost-effectiveness and being non-solvating. Recently, Jiang and co-workers have developed dimethoxyethane-based HCE diluted with FB for Li metal batteries. Their studies mainly focused on electrochemical stability in LillCu and Li-ion cells.<sup>29</sup> In comparison, our study not only focused on the electrochemical performance of FB-LHCE in Li-O2 cells but also comprehensively investigated the structures and properties of the FB-LHCE. We analyzed the solvation structure of electrolytes using Raman spectroscopy and determined the self-diffusivity coefficients of electrolyte components with the nuclear magnetic resonance (NMR) technique. Both analyses confirmed that FB remained as an inert solvent, which ceased coordinating with Li<sup>+</sup>. The influence of adding FB in HCE on various transport properties, including viscosity, ionic conductivity, and Li+ transference number, was also studied. Additionally, the impact of diluent on electrode wettability was investigated by contact angle and double-layer capacitance measurements. The ESWs were

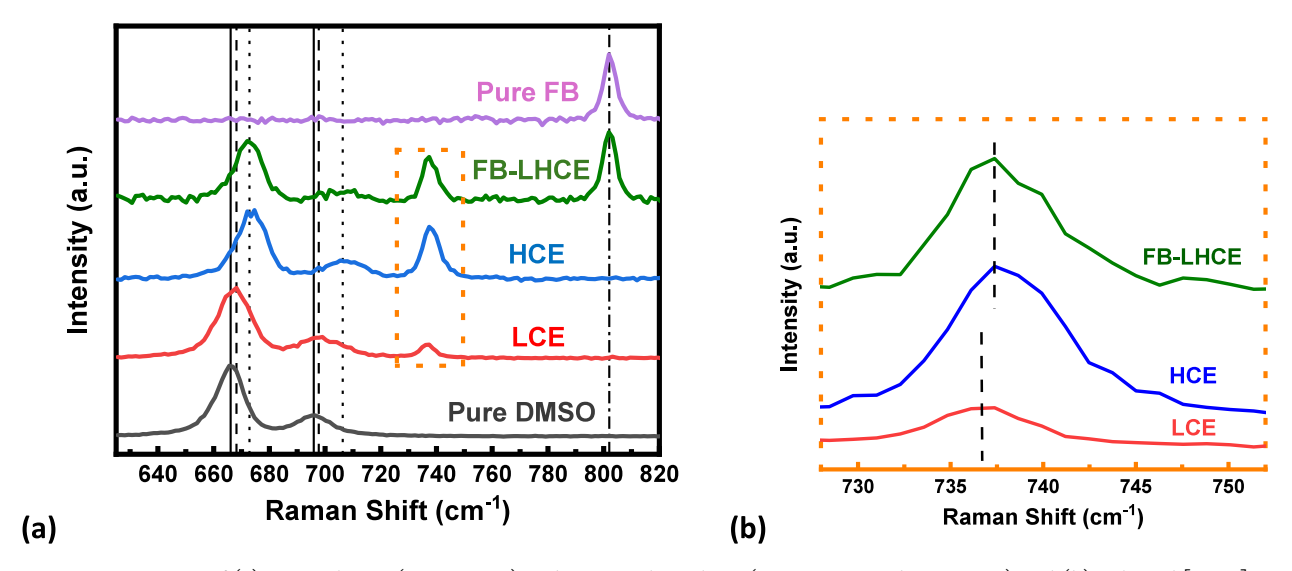


Figure 2. Raman spectra of (a) pure solvents (DMSO, FB) and various electrolytes (LCE, HCE, and FB-LHCE) and (b) enlarged [TFSI] anion region. Solid line (free DMSO), dashed line (partially coordinated), dotted line (fully coordinated), and dashed—dotted line (free FB).

determined by linear sweep voltammetry (LSV) technique. When compared with a low-concentration electrolyte (LCE) as the baseline, HCE and FB-LHCE have demonstrated wider anodic ESWs (>4.6 V). LillLi symmetric cell tests revealed significantly higher electrochemical stability of HCE and FB-LHCE (1300 h) with Li metal anode as compared with LCE (650 h). FB-LHCE achieved the highest deep discharge capacity (6.0 Ah g $^{-1}$ ), followed by LCE (2.25 Ah g $^{-1}$ ) and HCE (1.07 Ah g $^{-1}$ ) in the Li–O $_2$  cell. Full-cell cycling stability tests have shown enhanced cycling stability with FB-LHCE (11 cycles) compared with LCE (2 cycles) and HCE (2 cycles).

## 2. EXPERIMENTAL METHODS

**2.1. Electrolytes Preparation.** Dimethyl sulfoxide (DMSO, anhydrous >99.9%) and fluorobenzene (FB, >99.5%) were utilized as solvating and non-solvating organic solvents, respectively, in this study. Lithium bis(trifluoromethane)sulfonimide (LiTFSI, 99.95%) was exploited as a Li salt for electrolyte preparations. HCE was prepared by incorporating LiTFSI in DMSO with a 1:3 molar ratio. In order to prepare FB-LHCE, HCE was diluted with FB to achieve 1 M salt concentration. For comparison, baseline 1 M LiTFSI/DMSO was also prepared, which is denoted as LCE in this work. All commercial materials were purchased from Sigma-Aldrich and used as received in this study. All materials were opened and stored in an Ar-filled glovebox with H<sub>2</sub>O and O<sub>2</sub> levels < 0.1 ppm.

**2.2. Stability of Solvation Structure.** The stability of solvation structures of the three electrolytes, i.e., LCE, HCE, and FB-LHCE, was investigated by Raman spectroscopy. For this purpose, the electrolytes were soaked in a glass fiber separator inside the Ar-filled glovebox and placed and tightly sealed in glass vials. The electrolyte-soaked separators were exposed to the air just before the analysis under a Horiba Jobin Yvon LabRam ARAMIS Micro-Raman Microscope using 785 nm laser excitation. All measurements were repeated at least three times.

**2.3. Self-Diffusivity Coefficients.** Pulsed-field gradient stimulated echo nuclear magnetic resonance (PGSE-NMR) measurements were conducted to evaluate the self-diffusivity coefficients of LCE, HCE, and FB-LHCE. The experimental details can be found in the Supporting Information (Section S1: NMR Experimental Details).

**2.4. Physiochemical Properties Measurements.** The viscosities of LCE, HCE, and FB-LHCE were measured with a Brookfield DV-II+Pro viscometer. Galvanostatic EIS measurements were conducted with the SSISS symmetric cells to measure the effective ionic conductivity of the electrolytes in the glass fiber separator

material under compression (500 psi measured using a pressure gauge on a crimping machine) using a Biologic SP-150 potentiostat. Anodic ESWs of electrolytes were determined by the LSV technique at a scan rate of 10 mV s<sup>-1</sup> using LillSS cells. The Li<sup>+</sup> transference number of electrolytes was measured electrochemically using the potentiostatic polarization method. For this purpose, a constant voltage of 10 mV was applied for 400 s on LillLi symmetric cells. Electrochemical impedance spectroscopy (EIS) measurements were conducted before and after potentiostatic polarization in order to determine contact resistances in the frequency range 100 mHz to 500 kHz. Electric double-layer capacitance (EDLC) measurements were conducted using a cathodellcathode symmetric cell at open circuit voltage (OCV). The voltage was scanned in the voltage window of  $\pm 0.2$  V at a scan rate of 10 mV s<sup>-1</sup>. Static contact angle (CA) measurements of electrolytes were performed using a Ramé-Hart 190-U1 goniometer. Wettability measurements, EDLC, and CA measurements were conducted with a commercially available carbon cloth coated with a microporous layer (CT Carbon Cloth with MPL-W1S1011) purchased from the Fuel Cell Store.

**2.5. Porous Cathode Preparation.** Vulcan XC-72R coated carbon cloth was used as the porous cathode electrode in this study. The slurry was prepared by mixing Vulcan XC-72R with poly-(tetrafluoroethylene) (PTFE) binder (70:30 (wt %) ratio) in isopropyl alcohol (IPA) and water solution (70:30 (vol %) ratio) followed by sonication in a Branson bath sonicator. The mixture was sonicated for at least 3 h in order to achieve uniform dispersion. The prepared slurry was uniformly blade coated on 1071 HCB plain carbon cloth uniformly. The coated substrate was then dried for 24 h at room temperature in a fume hood, followed by heat treatment in a SentroTech furnace at 350 °C for 30 min. The electrodes were punched at 1.27 cm diameter for battery assembly. The measured carbon loading for each electrode of area 1.27 cm² was 0.95 ± 0.1 mg cm². Both Vulcan XC-72R and 1071 HCB carbon cloths were purchased from the Fuel Cell Store and utilized as received.

**2.6. Symmetric Cell and Full Cell Assembly.** Both full cells and symmetric cells were assembled in an Ar-filled Mikrouna glovebox with  $O_2$  and  $H_2O$  concentrations maintained below 0.1 ppm. For the  $\text{Li}-O_2$  full cell assembly, the as-prepared porous cathode was placed in the battery frame on the side engraved with the  $O_2$  channels. A Li chip (thickness, 0.25 mm; diameter, 1.27 cm) was utilized, which served as the anode. The electrodes were separated by an electrolyte-soaked Whatman glass fiber separator (GF/C, 1822-021; diameter, 1.58 cm). Each cell utilized 120  $\mu$ L of electrolyte. The battery was screwed appropriately to avoid leakage and exposure to the atmosphere. LillLi symmetric cell tests were conducted using coin cells.

Table 1. Self-Diffusivity Coefficients of Li<sup>+</sup>, [TFSI]<sup>-</sup>, DMSO, and FB in Various Electrolytes

Electrolyte	$Li^{+}$ (×10 <sup>-9</sup> $m^{2}$ $s^{-1}$ )	$[TFSI]^{-} (\times 10^{-9} \text{ m}^2 \text{ s}^{-1})$	DMSO $(\times 10^{-9} \text{ m}^2 \text{ s}^{-1})$	FB $(\times 10^{-9} \text{ m}^2 \text{ s}^{-1})$
LCE	0.1780	0.2533	0.3698	
HCE	0.0090	0.0110	0.0109	
FB-LHCE	0.2199	0.2058	0.2114	0.8534

2.7. Symmetric Cell and Full Cell Cycling. The assembled Li-O2 full cells were supplied continuously with 99.99% pure oxygen at a 1 atm pressure. Before beginning the tests, the battery was purged with oxygen for at least 1 h to stabilize the OCV and ensure the complete removal of Ar from the electrode assembly. Galvanostatic discharge/charge capacity tests were conducted on an 8-channel Neware BTS8.0 battery cycler. The electrochemical stability of electrolytes with a Li metal anode was determined by Li plating/ stripping tests in a LillLi symmetric cell in the absence of O2. The cell cycled for a fixed time of 1 h at 0.1 mA cm<sup>-2</sup> in each Li plating and stripping cycle. Full cell cycling stability tests were performed with a controlled capacity of 1.0 Ah  $\tilde{g}^{-1}$ . The cutoff voltages for discharging and charging used were 2.0 and 4.6 V, respectively. All battery cycling tests were conducted at a current density of 0.1 mA cm<sup>-2</sup> and room temperature. All tests were repeated at least three times. The reported specific capacities (Ah  $g^{-1}$ ) are based on the weight of active cathode material, i.e., Vulcan XC-72R in this study.

**2.8. Material Characterization.** In order to examine the morphology of the discharge product, discharged cathodes using the FB-LHCE electrolyte were analyzed under Hitachi SU8230 field emission scanning electron microscope (SEM). The composition of the discharge product was examined by a PHI 5000 Versa Probe II X-ray photoelectron spectroscopy (XPS) analysis.

#### 3. RESULTS AND DISCUSSION

3.1. Solvation Structure of Electrolytes. 3.1.1. Raman Spectroscopy. The solvation structures of LCE, HCE, and FB-LHCE were investigated by using Raman spectroscopy. For comparison, Raman spectra of pure DMSO and FB were also recorded. Figure 2a shows the Raman spectra of various electrolytes and pure solvents. For pure DMSO, two peaks appeared at 666 and 695 cm<sup>-1</sup>, which correspond to C- S symmetric and asymmetric stretching modes of DMSO, respectively.<sup>7,30</sup> At 1 M salt concentration (LCE), a slight shift of peaks to higher wavenumbers, i.e., 668 and 699 cm<sup>-1</sup> for C-S symmetric and asymmetric stretching bands of DMSO were recorded. This is ascribed to the coordination of DMSO molecules with Li<sup>+</sup> to form [Li(DMSO)<sub>n</sub>]<sup>+</sup> complexes in the solution.<sup>31</sup> Since solvent molecules significantly outnumber Li<sup>+</sup> cations, most DMSO molecules exist as free solvent molecules in LCE. Generally, at lower salt concentrations, each Li+ cation is coordinated with 4 DMSO molecules, i.e., [Li(DMSO)<sub>4</sub>]<sup>+,32</sup> This indicates that Li<sup>+</sup>-DMSO coordinated complex exists as a monodentate ligand; i.e., each DMSO molecule is bound to one Li<sup>+</sup> cation due to the presence of only one oxygen atom in its structure.<sup>33</sup> Additionally, with the incorporation of LiTFSI in DMSO, a new peak appeared at 736.5 cm<sup>-1</sup>, which is assigned to the S-N stretching mode of the [TFSI] anion. At a diluted state, [TFSI] anions generally exist as free ions and do not participate in coordination.<sup>31</sup> This is attributed to the different donor numbers of DMSO and [TFSI] anion. Since the Li+ cation is a strong Lewis acid, it prefers to interact with a strong Lewis base. DMSO has a significantly higher DN (29.8) than [TFSI] anion (7);<sup>34</sup> therefore, DMSO exhibits high electronpair donating ability and stronger affinity toward Li<sup>+</sup>. Consequently, the coordination structure exists as SSIP.<sup>32</sup>

For HCE, a prominent shift of C–S symmetric and asymmetric stretching modes of DMSO to even higher wavenumbers, i.e., 673 and 706 cm<sup>-1</sup>, was detected. Furthermore, the peak position of the band corresponds to the S–N stretching mode of [TFSI]<sup>-</sup> also shifted to a higher wavenumber, i.e., 737.5 cm<sup>-1</sup>, as indicated in Figure 2b.

This indicates that an entirely different coordinated structure of Li salt and DMSO is formed in HCE compared to LCE. 33 The increase in salt concentration also increases the concentration of coordinated DMSO molecules and decreases the uncoordinated DMSO molecules. 15 Previous reports indicate that all DMSO molecules are coordinated with Li+ with the increased salt concentration in HCE. 36,37 The increased salt concentration also increased the concentration of [TFSI] anions in the solution, which is evident from the higher peak intensity, shown in Figure 2b. Due to the scarcity of free DMSO molecules and increase in the [TFSI]concentration, the coordination between Li+ and the [TFSI] anion becomes stronger. As a result [TFSI] anion breaks into the solvation sheath of [Li(DMSO)<sub>n</sub>]<sup>+</sup> complex and replaces one or two DMSO molecules to form CIP  $([Li(DMSO)_n]^+-[TFSI]^-)$  and AGG  $([Li(DMSO)_n]^+ [TFSI]^--[Li(DMSO)_n]^+)$  complexes. The peak shift of S-N stretching mode of [TFSI] to a higher wavenumber in HCE indicates the formation of CIP and AGG. 32,38,39

For FB-LHCE, the C–S symmetric and asymmetric stretching bands of DMSO were observed at the wavenumber identical to that of HCE (i.e., 673 and 706 cm<sup>-1</sup>). Moreover, the band assigned to the S–N stretching mode of [TFSI]<sup>-</sup> also appeared at the same wavenumber as that of HCE. In addition to these peaks, a fourth peak at 802 cm<sup>-1</sup> was observed and assigned to free FB molecules.<sup>29</sup> For comparison, the Raman spectrum of pure FB solvent was also recorded, which confirmed the presence of uncoordinated FB molecules in FB-LHCE. It is evident from the Raman spectrum of FB-LHCE that the incorporation of diluent in HCE did not disrupt the coordination structures of Li<sup>+</sup>, [TFSI]<sup>-</sup>, and DMSO.

3.1.2. PGSE-NMR Spectroscopy. The stabilities of the solvation structures of Li<sup>+</sup> and DMSO were also investigated by measuring the self-diffusion coefficients of electrolyte components in LCE, HCE, and FB-LHCE using NMR. Figures S1, S2, and S3 in the Supporting Information show the diffusion coefficient measurement plots for each component in electrolyte solutions. Comprehensive information regarding data acquisition and processing can be found in the Supporting Information. The measured self-diffusivity coefficients of Li<sup>+</sup>, [TFSI]<sup>-</sup>, DMSO, and FB are shown in Table 1.

In LCE with 1 M salt concentration, the self-diffusivity coefficients determined follow the order  $D_{\rm DMSO} > D_{\rm [TFSI]}^{-} > D_{\rm Li}^{+}$ , which is in agreement with the previous reports. Although Li<sup>+</sup> exhibits the smallest ionic size among other electrolyte components, the lowest diffusivity coefficient suggests that it no longer exists as an independent Li<sup>+</sup> in the solution. Instead, it exists as solvated  $[{\rm Li}({\rm DMSO})_4]^+$  complex,

which has the largest hydrodynamic radius and, therefore, the smallest diffusivity coefficient. <sup>32,43</sup> The highest diffusivity coefficient measured for DMSO shows that significant amounts of uncoordinated molecules are present at lower salt concentrations and diffuse faster than their solvated counterparts. In HCE, the diffusivity coefficients of solution components are drastically decreased by over 1 order of magnitude. This is attributed to the increased viscosity and mass transfer resistance due to increased salt concentration. <sup>43</sup> Besides lowered diffusion coefficients obtained for HCE, a significant shift was observed in the relative difference of measured values of diffusion coefficients among all three electrolyte components. Contrary to LCE, the diffusion coefficients of Li<sup>+</sup>, [TFSI]<sup>--</sup>, and DMSO are quite close to each other, as shown in Figure 3. The increase in salt

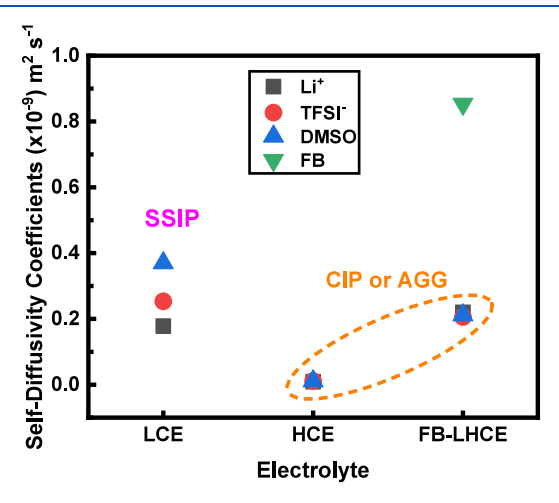


**Figure 3.** Comparison of the self-diffusivity coefficients of various components of LCE, HCE, and FB-LHCE.

concentration causes depletion of free DMSO molecules and enhanced coordination of Li<sup>+</sup> with the [TFSI]<sup>-</sup> anion. This indicates that all three components are coordinated and exist as either CIP or AGG complexes in the solution. In FB-LHCE, the diffusivity coefficients of Li+, [TFSI]-, and DMSO are enhanced substantially due to decreased viscosity. 17 Nevertheless, the diffusivity coefficients determined are almost identical for all three components. Evidently, these three components are well-coordinated even after the addition of a diluent and distributed among FB molecules in the form of clusters of CIP or AGG complexes. The non-solvating diluent causes fragmentation of the continuous solvation structure of coordinating ions and molecules. 25,35 This prolongs the lifetime of clusters comprised of Li<sup>+</sup>, [TFSI]<sup>-</sup> and DMSO. As a result, the components of clusters remain intact and diffuse together as one solvation shell over longer distances, as elucidated by the self-diffusivity coefficients of FB-LHCE. Moreover, FB molecules exhibit a considerably higher diffusivity coefficient than other complexes in the FB-LHCE

electrolyte, which indicates their presence as free and uncoordinated molecules in the solution.<sup>43</sup>

**3.2. Physiochemical Properties of Electrolytes.** The physiochemical properties of an electrolyte greatly influence the battery's performance. Transport properties, such as viscosity, ionic conductivity, and diffusivity, are critical to achieving a superior battery performance. Consequently, it is essential to tune these properties of electrolytes to render them suitable for the longevity of stable battery operation. We have measured various physiochemical properties, including viscosity, ionic conductivity, Li<sup>+</sup> transference number (t<sub>+</sub>), ESW, and wettability measurements of electrolyte systems under study. Table 2 summarizes the measured physicochemical properties of LCE, HCE, and FB-LHCE.

It is quite evident from the viscosity measurements that, with the increase in Li salt concentration, the electrolyte viscosity increases drastically for HCE. This is ascribed to the substantial rise in the number of  $[TFSI]^-$  anions, which leads to smaller distances and stronger Coulombic interactions with solvated  $[Li(DMSO)_n]^+$  complexes in the solution. Adding an inert cosolvent, FB, to HCE substantially reduced the viscosity by about 98%. Additionally, FB-LHCE is less viscous than LCE despite having the same overall salt concentration.

Any change in the electrolyte viscosity significantly impacts the diffusivity of electrochemical moieties due to variations in the mass transfer resistance. Mathematically, the Stokes—Einstein equation relates viscosity and diffusivity as follows:<sup>44</sup>

$$D = \frac{kT}{6\pi\eta r} \tag{2}$$

Here D,  $\eta$ , and r represent the diffusivity coefficient, viscosity, and radius of the diffusing species. The diffusivity is inversely related to the viscosity and hydrodynamic radius of the diffusing entity. As discussed in the previous section, the measured self-diffusivity coefficients of the electrolytes followed this behavior.

The ionic conductivity of the electrolytes was determined by EIS measurements. The Nyquist plots obtained for electrolyte solutions and equivalent circuit model (ECM) are shown in Figure S4 in the Supporting Information. The ionic conductivity of electrolytes is greatly influenced by the salt concentration. Previous studies have shown that ionic conductivity generally increases when salt concentration increases in the range of 0-1 M and demonstrates maximum ionic conductivity at 1 M salt concentration.<sup>45</sup> This is attributed to the increased number of charge transporting species. As the salt concentration exceeds 1 M, the number of charge-carrying species increases with a simultaneous rise in viscosity. Consequently, the ionic conductivity of HCE plunged to 1.18 mS cm<sup>-1</sup> compared to LCE (5.18 mS cm<sup>-1</sup>). A pronounced enhancement in ionic conductivity was recorded when FB was incorporated into the HCE due to a substantial decrease in viscosity. Figure 4a illustrates the trend of viscosity and ionic conductivity measured for the three

Table 2. Various Physiochemical Properties of LCE, HCE, and FB-LHCE Electrolytes

Electrolyte	Viscosity (cP)	Ionic Conductivity (mS cm <sup>-1</sup> )	$t_+^{\mathrm{NMR}}$	$t_{\scriptscriptstyle +}^{ m EC}$	Anodic ESW (V)	Contact Angle on MPL (deg)	$C_{\rm dl}~(\mu { m F})$
LCE	3.93	$5.12 \pm 0.7$	0.41	0.75	4.25	$130 \pm 2$	$6.77 \times 10^{-3}$
HCE	118.1	$1.18 \pm 0.32$	0.45	0.35	4.70	$120 \pm 2$	$1.84 \times 10^{-5}$
FB-LHCE	2.87	$6.00 \pm 0.41$	0.51	0.49	4.60	$20 \pm 2$	1.079

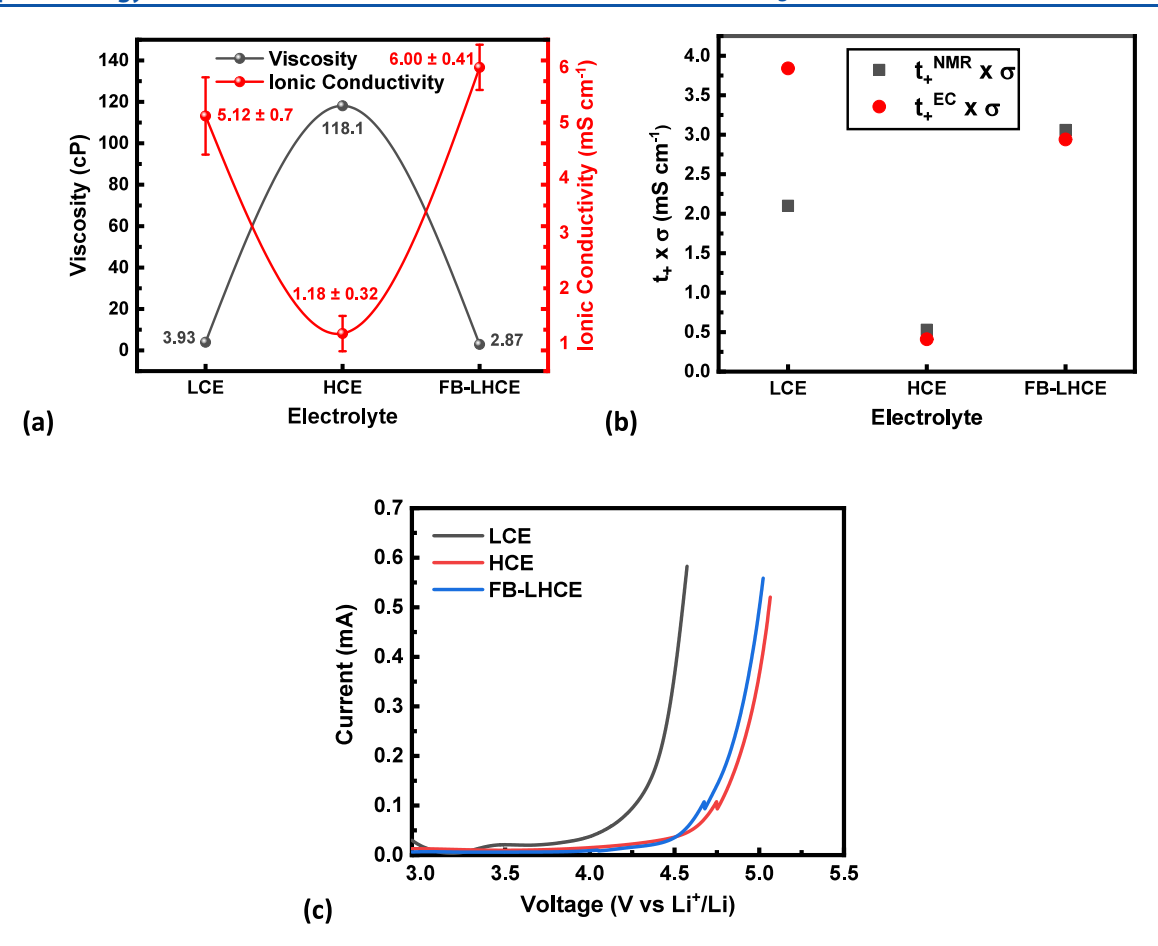


Figure 4. (a) Behavior of viscosity and ionic conductivity of electrolytes. (b) Comparison of Li<sup>+</sup>-ion conductivity calculated on the basis of  $t_+^{\text{NMR}}$  and  $t_+^{\text{EC}}$ . (c) Comparison of the anodic stability windows.

electrolytes. It is worth mentioning that the viscosity of HCE is increased by 30-fold when compared with LCE; nonetheless, the ionic conductivity is reduced by only 4.3 times. Similarly, when HCE is diluted with cosolvent FB, a 41-fold reduction in viscosity and a mere 5-fold increment in ionic conductivity were observed. This discrepancy shows that ionic conductivity is not simply inversely related to viscosity. The Walden rule correlates viscosity and conductivity as follows:<sup>46</sup>

$$\Lambda \eta^{\alpha} = C \tag{3}$$

$$\Lambda = \sigma \frac{M}{\rho} \tag{4}$$

Here,  $\Lambda$ ,  $\eta$ ,  $\alpha$ , C,  $\sigma$ , M, and  $\rho$  represent molar conductivity, viscosity, slope of the Walden plot, temperature-dependent constant, ionic conductivity, molecular weight, and density, respectively. Previous studies in literature have shown that the product of viscosity and molar conductivity is not constant with salt concentration or with the addition of cosolvent. This indicates that at higher salt concentrations ionic conductivity is considerably affected by more complex salt and solvent interactions besides viscosity.

Ionic conductivity measures the total amount of current carried by charge carriers in an electrolyte, which includes [TFSI]<sup>-</sup> anions, as well. Transference number measures the fraction of ionic current carried by specific species in a system. It is also a measure of the "quality" of ionic current generated by an electrolyte. <sup>49</sup> The ionic conductivity is often described in

terms of electrophoretic mobilities, and concentrations of ionic species present in an electrolyte system. 50

$$\sigma = F \sum_{i} z_{i} \mu_{i} c_{i} = F(z_{+} \mu_{+} c_{+} + z_{-} \mu_{-} c_{-})$$
(5)

Here F,  $z_v$ ,  $\mu_v$  and  $c_i$  represent Faraday's constant, charge, mobility, and concentration of species i, respectively. The transference number of cationic species can be calculated  $c_s^{43,50,51}$ 

$$t_{+} = \frac{z_{+}\mu_{+}c_{+}}{z_{+}\mu_{+}c_{+} + z_{-}\mu_{-}c_{-}}$$
(6)

Assuming the electrolyte to be electroneutral  $(\sum z_i c_i = 0)$ , the equation presented above reduces to the following equation:

$$t_{+} = \frac{\mu_{+}}{\mu_{+} + \mu_{-}} \tag{7}$$

For an infinitely dilute, ideal solution with completely dissociated salt, the electrophoretic mobility can be related to the diffusion coefficient by using the Nernst–Einstein equation as follows:

$$\mu_i = \frac{D_i z_i F}{RT} \tag{8}$$

Here  $D_i$ , R, and T represent the self-diffusivity coefficient of species i, the ideal gas constant, and temperature, respectively. Substitution of eq 8 into eq 7 yields the equation that is used to determine the transference number of the electrolyte.

$$t_{+}^{\text{NMR}} = \frac{D_{+}}{D_{+} + D_{-}} \tag{9}$$

Here  $t_+^{\rm NMR}$  denotes the transference number calculated by self-diffusivity coefficients of cations and anions determined by NMR.  $D_+$  and  $D_-$  represent self-diffusivity coefficients of the cation and anion, respectively. Values of the transference numbers calculated based on the self-diffusivity coefficients measured by NMR are summarized in Table 2. Based on self-diffusivity coefficients, the Li<sup>+</sup> transference numbers calculated for the three electrolytes are in the order FB-LHCE > HCE > LCE. The enhancement in  $t_+^{\rm NMR}$  of electrolyte with salt concentration is in accordance with the previous reports. <sup>52,53</sup>

We also measured Li<sup>+</sup> transference number using the potentiostatic polarization method established by Bruce and Vincent.<sup>54</sup> The chronoamperometric and EIS plots for LCE, HCE and FB-LHCE are shown in Figure S5 in the Supporting Information. The cationic transference number is given by the following equation:

$$t_{+}^{\text{EC}} = \frac{I_{\text{ss}}(\Delta V - I_0 R_0)}{I_0(\Delta V - I_{\text{ss}} R_{\text{ss}})}$$
(10)

Here  $I_0$  is the initial current,  $I_{\rm ss}$  the steady-state current,  $\Delta V$  the applied potential, and  $R_0$  and  $R_{\rm ss}$  represent electrode resistances before and after polarization, respectively.

Li<sup>+</sup> transference numbers measured for LCE, HCE, and FB-LHCE are 0.75, 0.35, and 0.49, respectively, which follow the order LCE > FB-LHCE > HCE. This discrepancy in the transference number measured with self-diffusivity coefficients and electrochemical method were also reported by other groups. 52,55,56 Self-diffusivity coefficients determined by NMR contain contributions from uncoordinated ions as well as coordinated ions, which exist in the form of ion pairs. They are greatly influenced by solvation structures, ion associations, and viscosity of the electrolyte. Consequently,  $t_+^{\rm NMR}$  obtained for electrolytes may provide overestimated values owing to the presence of ion pairs.  $^{57}$   $t_{+}^{\rm NMR}$  increases with salt concentration, which could be ascribed to the high concentration of anions. The transference numbers estimated by the electrochemical method only detect migration and diffusion of free ions, and as a result, LCE yielded the highest transference number. With the increase in salt concentration and the emergence of a new solvation structure, the number of free ions significantly reduced, which led to the lower value of transference number in HCE.<sup>57</sup> The increase in transference number was recorded when HCE was diluted with FB. Previous reports have suggested that the addition of small amounts of inert solvent to HCE generally causes a decrement in transference number primarily due to discontinuity in the long continuous network of Li<sup>+</sup>-solvent complexes. However, when HCE is diluted to much lower concentrations like 1 mol L<sup>-1</sup>, an increase in transference number was reported, which is in line with the current study.<sup>58</sup> It is worth noting that transference numbers obtained for FB-LHCE with NMR and polarization method are quite close to each other, i.e., 0.51 and 0.49, respectively, as opposed to LCE and HCE. In an ideal solution, at infinite dilution, the transference number measured by NMR and electrochemical method should be equivalent to each other; i.e.,  $t_{+}^{NMR} = t_{+}^{EC.58}$  This implies that FB-LHCE exhibits properties close to those of an ideal solution. Figure 4b shows the comparison of Li<sup>+</sup>-ion conductivity  $(t_+ \times \sigma)$ 

calculated based on the transference numbers obtained from two methods.

The anodic ESWs of electrolytes were determined by the LSV technique. Figure 4c shows the comparison of anodic stability limits of LCE, HCE, and FB-LHCE. It is evident that both HCE and FB-LHCE displayed broader anodic stability limits than LCE. The enhanced oxidative stability of HCE could be ascribed to the scarcity of uncoordinated DMSO molecules in its solvation structure. The coordinated  $[\text{Li}(\text{DMSO})_n]^+$  complexes exhibit lower highest occupied molecular orbital (HOMO) energy than uncoordinated solvent molecules which are prone to degradation at higher voltages. The coordinated solvent molecules which are prone to degradation at higher voltages.

The wettability of an electrolyte with a porous cathode is a critical parameter that controls the distribution of electrolyte on the electrode surface. We elucidated the wettability of LCE, HCE, and FB-LHCE by measuring the static contact angles on the porous electrode surface as well as double-layer capacitance measurements, as shown in Figure S6 and S7, respectively in the Supporting Information. The contact angles measured for LCE, HCE, and FB-LHCE are  $130 \pm 2$ ,  $120 \pm 2$ , and  $20 \pm 2^{\circ}$ , respectively. Both LCE and HCE exhibit lyophobic properties, as illustrated by their contact angles. DMSO is known to have high surface tension (43 mN m<sup>-1</sup>), which rendered LCE to yield the highest contact angle.<sup>59</sup> Increasing salt concentration caused a decrease in surface tension, which led to lower contact angle measurement, as demonstrated by HCE.<sup>60</sup> FB-LHCE, on the other hand, displayed strong lyophilic behavior. During contact angle measurements, it was observed that FB-LHCE instantly absorbed into the electrode surface, unlike its counterparts. Evidently, the addition of FB to HCE drastically improved the wettability of the electrolyte. Although contact angle provides information about the wettability of electrolytes on an electrode surface, the behavior of electrolyte distribution inside the electrode and quantification of solid-liquid interfacial area needs to be investigated with double-layer capacitance measurements  $(C_{\rm dl})$ . Consequently, the  $C_{\rm dl}$  of electrolytes was determined electrochemically using symmetric cathodellcathode cells. Figure S7 compares  $C_{\rm dl}$  curves obtained for LCE, HCE, and FB-LHCE. FB-LHCE demonstrated the highest  $C_{\rm dl}$  (1.079) followed by LCE (6.77 × 10<sup>-3</sup>) and HCE  $(1.84 \times 10^{-5})$ . Owing to its extreme lyophilic behavior, FB-LHCE achieved 3 and 5 orders of magnitude higher  $C_{dl}$ compared to LCE and HCE, respectively. An electric double layer is formed on the wetted surface of the electrode. Higher values of C<sub>dl</sub> represent an electrolyte that is able to wet a greater area of an electrode. C<sub>dl</sub> is related to the wetted solidliquid interfacial area by the following equation:<sup>61</sup>

$$C_{\rm dl} = \varepsilon_{\rm r} \varepsilon_{\rm o} \frac{A_{\rm sl}}{d} \tag{11}$$

Here  $\varepsilon_{\rm r}$  represents the relative permittivity of an electrolyte,  $\varepsilon_{\rm o}$  is the permittivity of the vacuum, d denotes the double-layer thickness, which is estimated by debye length, and  $A_{\rm sl}$  represents the area of the wetted pore surface. For a given electrolyte at room temperature,  $\varepsilon_{\rm r}$ ,  $\varepsilon_{\rm o}$ , and d can be considered as constants. Therefore, the area of the wetted pore surface is proportional to the double-layer capacitance.

FB-LHCE yielded the highest  $C_{\rm dl}$  value, which means that the possibility of the formation of triphase boundaries in the porous electrode is significantly higher than for its counterpart. Internal wettability of an electrolyte profoundly impacts the creation of triphase boundaries, i.e., cathode surface—electro-

lyte– $O_2$  gas boundaries, which enable the electrochemical reaction to occur during the discharge cycle. Low  $C_{\rm dl}$  values, as yielded by LCE and HCE, represent poor wettability and the absence of adequate triphase boundaries to achieve high discharge capacity. This adversely affects the discharge performance of the Li– $O_2$  battery as the majority of the electrode area is devoid of electrolyte and therefore remains an inactive electrochemical site. A more detailed picture of battery performance is presented in the subsequent section.

**3.3. Symmetric Cell and Full Cell Performance.** The stability of electrolytes relative to the Li metal anode was investigated by LillLi symmetric cell cycling. The voltage profiles of LCE, HCE, and FB-LHCE electrolytes with respect to time are shown in Figure 5. It is evident that the stability of

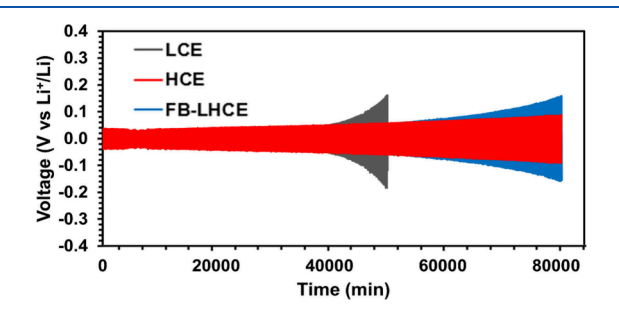


**Figure 5.** Voltage profiles of Li plating/stripping in LillLi symmetric cells cycled at a current density of  $0.1~\text{mA}~\text{cm}^{-2}$  with LCE, HCE, and FB-LHCE.

Li plating/stripping was greatly enhanced with HCE and FB-LHCE compared with LCE. This indicated the formation of a

stable SEI layer on the Li surface, which enabled stable cycling for a longer period of time. The cell with LCE demonstrated increased polarization after 650h (39000 min), which reflected the formation of an unstable SEI layer with the diluted electrolyte. In contrast, FB-LHCE displayed lower overpotential until around 1300h (78000 min). HCE exhibited the lowest polarization with the most stable cycling. However, the higher viscosity and lower ionic conductivity impede its application in full-cell cycling. The improved interfacial stability of HCE with the Li metal anode can be attributed to the formation of an anion-derived SEI layer owing to the shift in lowest unoccupied molecular orbital (LUMO) energy levels from solvents to anion. Anion-derived SEI layers are robust, inhibit the decomposition of solvents and Li dendrite formation, and effectively enhance the Li plating/stripping process.<sup>35</sup> Furthermore, Jiang and co-workers reported a LiF-SEI layer with FB-diluted HCE as compared with conventional electrolyte, which effectively alleviates the parasitic reactions with fresh Li metal and electrolyte owing to its good insulating properties. Additionally, FB-diluted HCE was found to inhibit Li dendrite formation during Li plating and stripping by producing highly compact and less porous Li films. The deposited Li films with high porosity and specific surface areas promote a high degree of electrolyte decomposition by allowing the electrolyte to be absorbed and react with fresh Li metal underneath it. They also showed that FB-diluted HCE greatly suppressed the decomposition of solvating solvents compared with conventional electrolytes. Therefore, electrolyte stability with Li metal anode is critical to achieving long-term cycling of Li-O<sub>2</sub> full cell.<sup>29</sup>

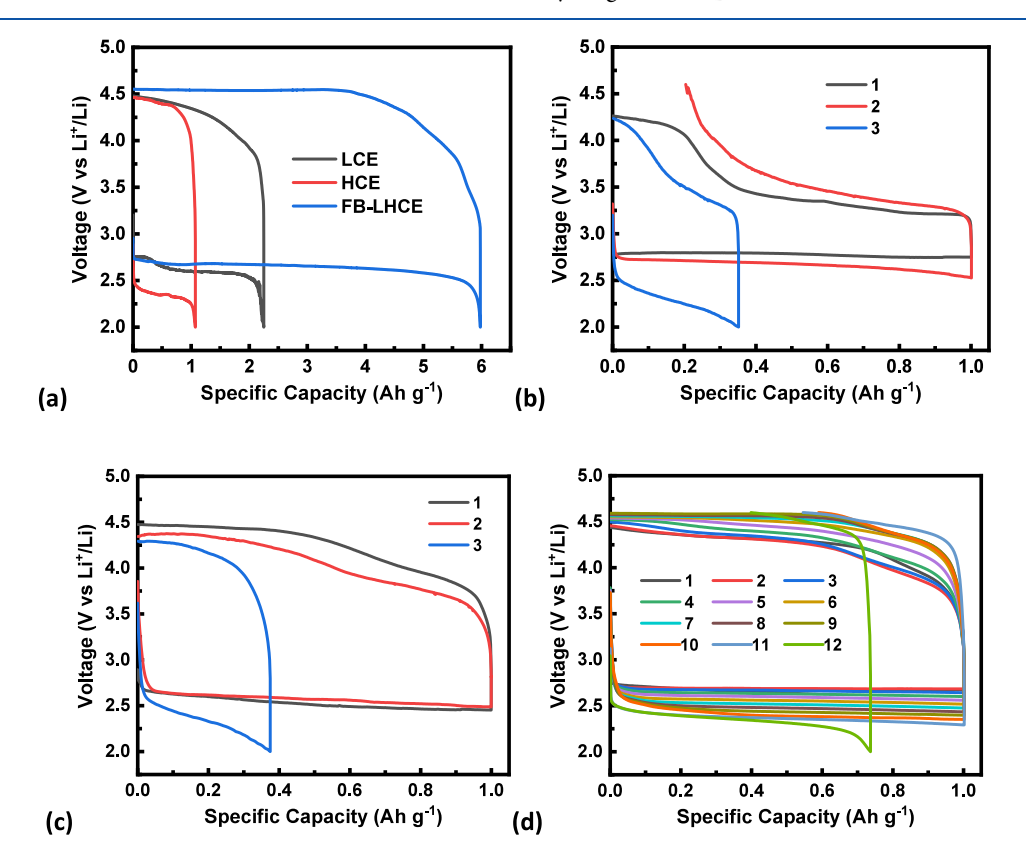


Figure 6. (a) Comparison of deep discharge capacity obtained with LCE, HCE, and FB-LHCE. Limited capacity cycling stability plots for (b) LCE, (c) HCE, and (d) FB-LHCE. All tests were conducted at a current density of 0.1 mA cm<sup>-2</sup>.

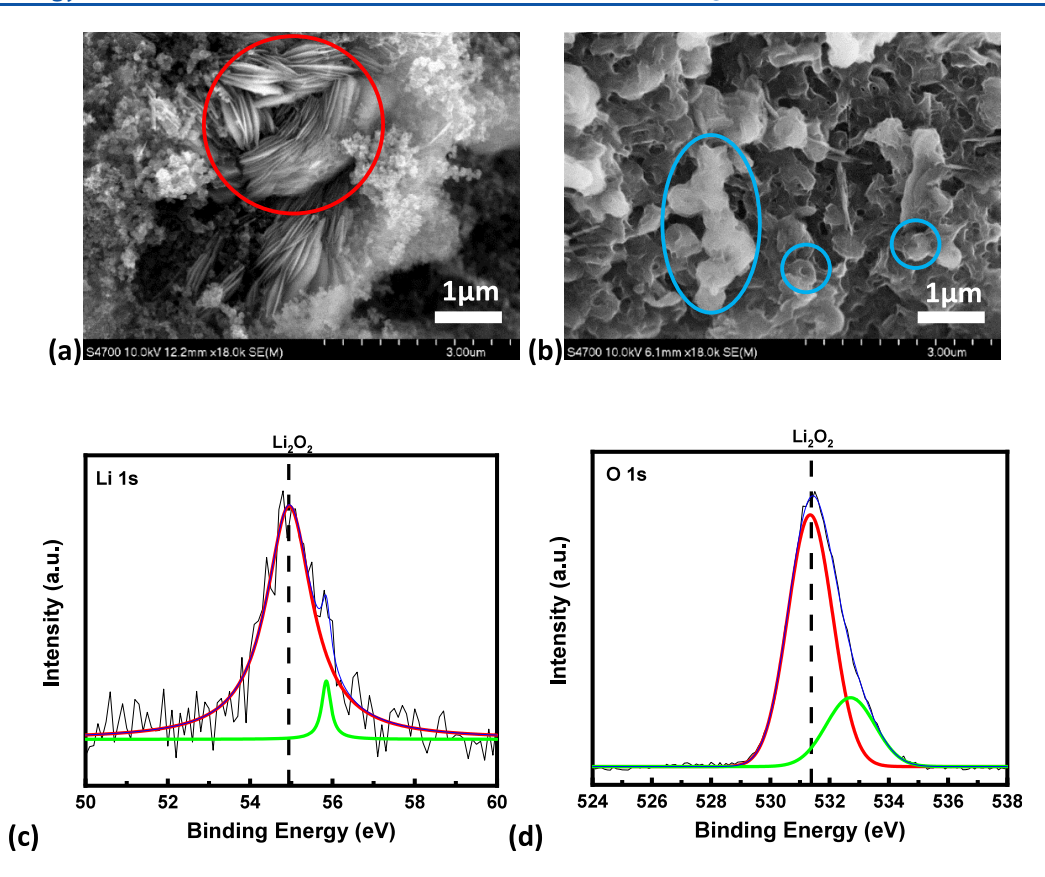


Figure 7. SEM images of a porous cathode with FB-LHCE (a) discharged to the limited capacity of 1.0 Ah g<sup>-1</sup> and (b) deeply discharged until the reaction stops. XPS profiles of the porous cathode deeply discharged with FB-LHCE: (c) Li 1s and (d) O 1s spectra.

Full cell galvanostatic discharge/charge cycling was performed with LCE, HCE, and FB-LHCE electrolytes at 0.1 mA cm<sup>-2</sup> current density. Figure 6a compares the deep discharge capacities obtained with the aforementioned electrolytes. FB-LHCE achieved the highest specific discharge capacity (6.0 Ah g<sup>-1</sup>) followed by LCE (2.25 Ah g<sup>-1</sup>) and HCE (1.07 Ah g<sup>-1</sup>). The discharge capacity obtained with FB-LHCE is nearly 6 times greater than HCE. This could be ascribed to the improved electrode wettability and enhanced transport properties, i.e., the incorporation of diluent significantly reduced viscosity and increased ionic conductivity. It is worth noting that high salt concentration yielded low discharge voltage, which is consistent with the previous reports. 45 The operating discharge voltage for HCE is <2.5 V. This could be ascribed to its high mass transfer resistance and sluggish kinetics owing to its high viscosity. On the other hand, FB-LHCE demonstrates a stable discharge voltage of around 2.7 V, which is indicative of its enhanced transport properties.

Although LCE displayed transport properties comparable to FB-LHCE, the poor wettability, as evidenced by double-layer capacitance measurement, resulted in a smaller number of triphase boundaries and consequently less discharge product and discharge capacity. The discharge voltage for LCE is much closer to that of FB-LHCE than HCE owing to its superior transport properties. In addition to transport properties, the discharge voltage is directly affected by the interfacial concentration of reactant ions as per the Nernst equation. <sup>45,63</sup> At open circuit voltage (OCV), Li<sup>+</sup> ions fully occupy the cathode—electrolyte interphase as a reactant species. The interfacial concentration of Li<sup>+</sup>-ions is contingent on the size of

their solvated shell. As mentioned in the previous section, Li<sup>+</sup>ions exist as SSIP ( $[Li(DMSO)_n]^+$ ) at lower salt concentrations, such as in LCE, which has a smaller hydrodynamic radius and therefore occupies less space on the cathode surface. On the contrary, Li+ ions exist as CIP ([Li- $(DMSO)_n]^+-[TFSI]^-)$  and AGG  $([Li(DMSO)_n]^+-[TFSI]^--[Li(DMSO)_n]^+)$  complexes at high salt concentrations, which exhibit much larger ionic radii as compared to SSIP. This results in the lower Li<sup>+</sup>-ions concentration at the cathode-electrolyte interphase. During the discharge reaction, when interfacial Li<sup>+</sup>-ions are consumed, the reduced species are replaced by new Li<sup>+</sup> ions from the bulk electrolyte to the electrode surface. This supply of Li<sup>+</sup> ions from electrolytes depends on their concentration and the speed with which they reach the surface. For HCE, the concentration of Li<sup>+</sup> ions in the solution is higher; nonetheless, the discharge voltage is lower, which could be ascribed to the lower diffusivity coefficient of Li<sup>+</sup> ions as measured by NMR and a larger complex size. Although the concentration of Li<sup>+</sup> ions is lower for LCE, the replenishment of Li<sup>+</sup> ions is much faster from the bulk electrolyte to the electrode surface, as indicated by their self-diffusivity coefficients. Moreover, due to their smaller size, more Li<sup>+</sup> ions can occupy the electrode surface area, which leads to a higher discharge voltage. In the case of FB-LHCE, although the hydrodynamic radius of the Li<sup>+</sup> solvation shell is similar to that of HCE, the self-diffusivity coefficient is significantly higher, allowing the Li<sup>+</sup> ions to reach the electrode surface in a much shorter time.

It is worth mentioning that the incorporation of FB, which is classified as a fluorinated diluent, to the HCE significantly increased the fluorine content in the electrolyte, which is linked to the increased  $O_2$  solubility in the electrolyte. <sup>64,65</sup> It is a well-established fact that oxygen is sparingly soluble in organic solvents such as DMSO, and its concentration in the electrolyte greatly impacts the performance of Li– $O_2$  batteries. The addition of FB to the DMSO-based HCE has therefore improved the solubility of  $O_2$  as it is known to interact favorably with the fluorocarbons. The significantly higher discharge capacity obtained by FB-LHCE can also be attributed to the enhanced  $O_2$  solubility.

In order to understand the cycling behavior of these electrolytes, full-cell cycling stability tests were performed with a curtailed capacity at 1.0 Ah g<sup>-1</sup>. Panels b-d of Figure 6 show the cycling stability plots of LCE, HCE, and FB-LHCE. It is evident from the cycling stability plots that FB-LHCE yielded the highest number of cycles, followed by LCE and HCE. The enhanced cycle life of Li-O2 battery using FB-LHCE can be attributed to its improved electrochemical stability, transport properties, O2 solubility, and electrode wettability. Conversely, the LCE sustained only two cycles. The excess of uncoordinated DMSO molecules in LCE is susceptible to attack by superoxide ions (O2-) generated during oxygen reduction reactions. This leads to the degradation of electrolyte and, consequently, battery cycling instability. Furthermore, the instability of DMSO with Li anode yields an unstable SEI layer, which fails to protect the Li surface for a longer period of time and causes limited cycling stability. Meanwhile, Li-O2 battery utilizing HCE with a stable solvation structure and high electrochemical and chemical stability also yielded only two cycles. High viscosity and poor wettability of HCE could be the prime factors affecting battery performance.

Although LCE displayed poor cycling performance, the charging overpotential is much lower than those of its counterparts, which could be ascribed to its good transport properties and faster kinetics. For the HCE, the increased cell polarization is attributed to high solution resistance and slower reaction rates. Interestingly, FB-LHCE demonstrated higher charge overpotentials despite exhibiting superior transport properties. Kwak and co-workers studied various fluorinated diluents with concentrated electrolytes and reported a charging voltage plateau at around 4.6–4.7 V.

In order to elucidate the morphology and composition of the discharge product generated with FB-LHCE, the discharged carbon electrodes were examined under SEM and XPS. Figure 7a shows an SEM image of a porous cathode discharged to the limited capacity of 1.0 Ah g<sup>-1</sup>. The discharge product can be viewed as accumulated in the form of long plate-like structures. These plate-like structures have arranged themselves so that they appear to form a substantially large flower-like structure embedded in Vulcan XC particles, as marked by the red circle. For comparison, the morphology of the discharge product in a deeply discharged cathode electrode was also analyzed. Figure 7b shows an SEM image of a deeply discharged porous cathode. The discharge product in the form of toroids is distributed on the cathode surface. The morphology of the discharge product has transformed significantly with the depth of discharge. Furthermore, the entirety of the cathode surface is covered with discharge product, which portrays that the majority of the electrode area was utilized during discharging, and the reaction stopped due to mass transfer limitations. This was not the case with the electrode with a limited capacity as the majority of electrode area was found unutilized.

The oxidation state of the discharge product was determined by using XPS analysis. Panels c and d of Figure 7 illustrate the XPS spectra of Li 1s and O 1s. The binding energy (BE) peaks for both spectra were deconvoluted in order to identify the composition of the discharge product. The deconvoluted BE peaks at 54.9 and 531.35 eV for Li 1s and O 1s spectra, respectively, and are in good agreement with the previous reports for Li<sub>2</sub>O<sub>2</sub>. 66,67 Diminished BE peaks that appeared at 55.8 and 532.67 eV for Li 1s and O 1s spectra, respectively, could be assigned to Li<sub>2</sub>CO<sub>3</sub>. Nonetheless, the majority of the discharge product formed on the cathode surface with FB-LHCE is Li<sub>2</sub>O<sub>2</sub>, which is desired for the enhanced cycling stability of the Li-O<sub>2</sub> battery.

## 4. CONCLUSION

We presented a comprehensive study of the electrochemical performance of a  $\text{Li}-\text{O}_2$  battery incorporated with FB diluted DMSO-based HCE. FB-LHCE outperformed LCE and HCE by achieving the highest discharge capacity, i.e., 6.0, 2.25, and 1.07 Ah g<sup>-1</sup>, respectively. Additionally, the cycling stability of full  $\text{Li}-\text{O}_2$  cells greatly improved with FB-LHCE (11 cycles) as compared to LCE (2 cycles) and HCE (2 cycles). The improved stability of FB-LHCE is attributed to its enhanced electrochemical stability with Li metal anode, its wider electrochemical stability window (>4.6 V), enhanced transport properties including low viscosity, high ionic conductivity and high self-diffusivity of its components, and superior electrode wettability that allows it to form a greater number of triphase boundaries in the oxygen electrode.

## ASSOCIATED CONTENT

#### Supporting Information

The Supporting Information is available free of charge at https://pubs.acs.org/doi/10.1021/acsaem.4c01566.

NMR experimental details; ionic conductivity measurements; Li<sup>+</sup> transference number measurement using electrochemical method; wettability measurements (PDF)

### AUTHOR INFORMATION

## **Corresponding Author**

Xianglin Li — Department of Mechanical Engineering, University of Kansas, Lawrence, Kansas 66045, United States; Department of Mechanical Engineering and Materials Science, Washington University in St. Louis, St. Louis, Missouri 63130, United States; ◎ orcid.org/0000-0002-0193-9410; Email: lxianglin@wustl.edu

## Authors

Syed Shoaib Hassan Zaidi — Department of Mechanical Engineering, University of Kansas, Lawrence, Kansas 66045, United States

Justin T. Douglas – Nuclear Magnetic Resonance Core Laboratory, University of Kansas, Lawrence, Kansas 66045, United States

Complete contact information is available at: https://pubs.acs.org/10.1021/acsaem.4c01566

### Notes

The authors declare no competing financial interest.

### ACKNOWLEDGMENTS

We highly appreciate the support from the National Science Foundation (Award Nos. 1941083 and 2329821).

## REFERENCES

- (1) Ren, M.; et al. Quasi-Solid-State Li-O2 Batteries with Laser-Induced Graphene Cathode Catalysts. *ACS Applied Energy Materials* **2020**, *3*, 1702–1709.
- (2) Policano, M. C.; Anchieta, C. G.; Nepel, T. C. M.; Filho, R. M.; Doubek, G. Water in Aprotic Li-O2 Batteries: A Critical Review. *ACS Applied Energy Materials* **2022**, *5*, 9228–9240.
- (3) Zhong, M.; Liu, M.; Li, N.; Bu, X.-H. Recent advances and perspectives of metal/covalent-organic frameworks in metal-air batteries. *Journal of Energy Chemistry* **2021**, *63*, 113–129.
- (4) Hassan Zaidi, S. S.; et al. Binder-free Li-O2 battery cathodes using Ni- and PtRu-coated vertically aligned carbon nanofibers as electrocatalysts for enhanced stability. *Nano Research Energy* **2023**, 2, No. e9120055.
- (5) Zaidi, S. S. H.; Li, X. Li–O2/Air Batteries Using Ionic Liquids A Comprehensive Review. *Adv. Energy Mater.* **2023**, *13*, No. 2300985.
- (6) McCloskey, B. D.; et al. Limitations in Rechargeability of Li-O2 Batteries and Possible Origins. *J. Phys. Chem. Lett.* **2012**, *3*, 3043–3047.
- (7) Togasaki, N.; Momma, T.; Osaka, T. Enhanced cycling performance of a Li metal anode in a dimethylsulfoxide-based electrolyte using highly concentrated lithium salt for a lithium-oxygen battery. *J. Power Sources* **2016**, *307*, 98–104.
- (8) Karkera, G.; Prakash, A. S. An Inorganic Electrolyte Li–O2 Battery with High Rate and Improved Performance. *ACS Appl. Energy Mater.* **2018**, *1*, 1381–1388.
- (9) Freunberger, S. A.; et al. Reactions in the Rechargeable Lithium—O2 Battery with Alkyl Carbonate Electrolytes. *J. Am. Chem. Soc.* **2011**, *133*, 8040–8047.
- (10) Chen, Y.; Freunberger, S. A.; Peng, Z.; Bardé, F.; Bruce, P. G. Li–O2 Battery with a Dimethylformamide Electrolyte. *J. Am. Chem. Soc.* **2012**, *134*, 7952–7957.
- (11) Horwitz, G.; Calvo, E. J.; Méndez De Leo, L. P.; de la Llave, E. Electrochemical stability of glyme-based electrolytes for Li–O2 batteries studied by in situ infrared spectroscopy. *Phys. Chem. Chem. Phys.* **2020**, 22, 16615–16623.
- (12) Hassan Zaidi, S. S.; Sigdel, S.; Sorensen, C. M.; Kwon, G.; Li, X. Incorporation of Novel Graphene Nanosheet Materials as Cathode Catalysts in Li-O2 Battery. *J. Electrochem. Energy Convers. Storage* **2023**, *20*, 020907.
- (13) Iliksu, M.; et al. Elucidation and Comparison of the Effect of LiTFSI and LiNO3 Salts on Discharge Chemistry in Nonaqueous Li—O2 Batteries. ACS Appl. Mater. Interfaces 2017, 9, 19319—19325.
- (14) Liu, B.; et al. Stabilization of Li Metal Anode in DMSO-Based Electrolytes via Optimization of Salt—Solvent Coordination for Li—O2 Batteries. *Adv. Energy Mater.* **2017**, *7*, No. 1602605.
- (15) Pranay Reddy, K.; Fischer, P.; Marinaro, M.; Wohlfahrt-Mehrens, M. Improved Li-Metal Cycling Performance in High Concentrated Electrolytes for Li-O2 Batteries. *ChemElectroChem.* **2018**, *5*, 2758–2766.
- (16) Zheng, J.; Lochala, J. A.; Kwok, A.; Deng, Z. D.; Xiao, J. Research Progress towards Understanding the Unique Interfaces between Concentrated Electrolytes and Electrodes for Energy Storage Applications. *Advanced Science* **2017**, *4*, 1700032.
- (17) Watanabe, Y.; Ugata, Y.; Ueno, K.; Watanabe, M.; Dokko, K. Does Li-ion transport occur rapidly in localized high-concentration electrolytes? *Phys. Chem. Chem. Phys.* **2023**, *25*, 3092–3099.
- (18) Yamada, Y.; Yamada, A. Review—Superconcentrated Electrolytes for Lithium Batteries. J. Electrochem. Soc. 2015, 162, A2406.
- (19) Martins, M. L.; et al. Structure-Dynamics Interrelation Governing Charge Transport in Cosolvated Acetonitrile/LiTFSI Solutions. *J. Phys. Chem. B* **2023**, *127*, 308–320.

- (20) Kwak, W.-J.; et al. Effects of Fluorinated Diluents in Localized High-Concentration Electrolytes for Lithium—Oxygen Batteries. *Adv. Funct Mater.* **2021**, *31*, No. 2002927.
- (21) Chen, S.; et al. High-Voltage Lithium-Metal Batteries Enabled by Localized High-Concentration Electrolytes. *Adv. Mater.* **2018**, *30*, No. 1706102.
- (22) Ren, X.; et al. Localized High-Concentration Sulfone Electrolytes for High-Efficiency Lithium-Metal Batteries. *Chem.* **2018**, *4*, 1877–1892.
- (23) Ren, X.; et al. Enabling High-Voltage Lithium-Metal Batteries under Practical Conditions. *Joule* **2019**, *3*, 1662–1676.
- (24) Zhao, Q.; et al. Binary Mixtures of Highly Concentrated Tetraglyme and Hydrofluoroether as a Stable and Nonflammable Electrolyte for Li-O2 Batteries. ACS Appl. Mater. Interfaces 2018, 10, 26312–26319.
- (25) Kwak, W.-J.; et al. Optimized Electrolyte with High Electrochemical Stability and Oxygen Solubility for Lithium—Oxygen and Lithium—Air Batteries. *ACS Energy Lett.* **2020**, *5*, 2182–2190.
- (26) Dokko, K.; et al. Solvate Ionic Liquid Electrolyte for Li-S Batteries. J. Electrochem. Soc. 2013, 160, A1304.
- (27) Moon, H.; et al. Solvent Activity in Electrolyte Solutions Controls Electrochemical Reactions in Li-Ion and Li-Sulfur Batteries. *J. Phys. Chem. C* **2015**, *119*, 3957–3970.
- (28) Ueno, K.; et al. Li+ Solvation and Ionic Transport in Lithium Solvate Ionic Liquids Diluted by Molecular Solvents. *J. Phys. Chem. C* **2016**, *120*, 15792–15802.
- (29) Jiang, Z.; et al. Fluorobenzene, A Low-Density, Economical, and Bifunctional Hydrocarbon Cosolvent for Practical Lithium Metal Batteries. *Adv. Funct Mater.* **2021**, *31*, No. 2005991.
- (30) Xuan, X.; Wang, J.; Zhao, Y.; Zhu, J. Experimental and computational studies on the solvation of lithium tetrafluorobrate in dimethyl sulfoxide. *J. Raman Spectrosc.* **2007**, *38*, 865–872.
- (31) Leverick, G.; et al. Solvent- and Anion-Dependent Li+-O2-Coupling Strength and Implications on the Thermodynamics and Kinetics of Li-O2 Batteries. *J. Phys. Chem. C* **2020**, *124*, 4953–4967.
- (32) Tatara, R.; et al. Oxygen Reduction Reaction in Highly Concentrated Electrolyte Solutions of Lithium Bis-(trifluoromethanesulfonyl)amide/Dimethyl Sulfoxide. *J. Phys. Chem.* C 2017, 121, 9162–9172.
- (33) Yamada, Y.; Takazawa, Y.; Miyazaki, K.; Abe, T. Electrochemical Lithium Intercalation into Graphite in Dimethyl Sulfoxide-Based Electrolytes: Effect of Solvation Structure of Lithium Ion. *J. Phys. Chem. C* **2010**, *114*, 11680–11685.
- (34) Yamagata, M.; Katayama, Y.; Miura, T. Electrochemical Behavior of Samarium, Europium, and Ytterbium in Hydrophobic Room-Temperature Molten Salt Systems. *J. Electrochem. Soc.* **2006**, *153*, No. E5.
- (35) Cao, X.; Jia, H.; Xu, W.; Zhang, J.-G. Review—Localized High-Concentration Electrolytes for Lithium Batteries. *J. Electrochem. Soc.* **2021**, *168*, 010522.
- (36) Wang, L.; Uosaki, K.; Noguchi, H. Effect of Electrolyte Concentration on the Solvation Structure of Gold/LITFSI–DMSO Solution Interface. *J. Phys. Chem. C* **2020**, *124*, 12381–12389.
- (37) Qiao, Y.; et al. Li2CO3-free Li-O2/CO2 battery with peroxide discharge product. *Energy Environ. Sci.* **2018**, *11*, 1211–1217.
- (38) Hu, Y.-S.; Lu, Y. The Mystery of Electrolyte Concentration: From Superhigh to Ultralow. ACS Energy Lett. 2020, 5, 3633-3636.
- (39) Xu, S.; et al. Decoupling of ion pairing and ion conduction in ultrahigh-concentration electrolytes enables wide-temperature solid-state batteries. *Energy Environ. Sci.* **2022**, *15*, 3379–3387.
- (40) Yoshida, K.; Tsuchiya, M.; Tachikawa, N.; Dokko, K.; Watanabe, M. Change from Glyme Solutions to Quasi-ionic Liquids for Binary Mixtures Consisting of Lithium Bis-(trifluoromethanesulfonyl)amide and Glymes. J. Phys. Chem. C 2011, 115, 18384–18394.
- (41) Hayamizu, K.; Aihara, Y.; Arai, S.; Martinez, C. G. Pulse-Gradient Spin-Echo 1H, 7Li, and 19F NMR Diffusion and Ionic Conductivity Measurements of 14 Organic Electrolytes Containing LiN(SO2CF3)2. *J. Phys. Chem. B* **1999**, 103, 519–524.

- (42) Zhang, C.; et al. Chelate Effects in Glyme/Lithium Bis(trifluoromethanesulfonyl)amide Solvate Ionic Liquids. I. Stability of Solvate Cations and Correlation with Electrolyte Properties. *J. Phys. Chem. B* **2014**, *118*, 5144–5153.
- (43) Bergstrom, H. K.; McCloskey, B. D. Ion Transport in (Localized) High Concentration Electrolytes for Li-Based Batteries. ACS Energy Lett. 2024, 9, 373–380.
- (44) Zaidi, S. S. H.; Kore, R.; Shiflett, M. B.; Li, X. Effects of operating temperature on Li-O2 battery with ionic liquid-based binary electrolyte. *Electrochim. Acta* **2024**, *473*, No. 143494.
- (45) Jiang, J.; et al. The influence of electrolyte concentration and solvent on operational voltage of Li/CFx primary batteries elucidated by Nernst Equation. *J. Power Sources* **2022**, *527*, No. 231193.
- (46) Walden, P. Über organische Lösungs- und Ionisierungsmittel. III. Teil: Innere Reibung und deren Zusammenhang mit dem Leitvermögen 1906, 55U, 207–249.
- (47) Yamada, Y.; Wang, J.; Ko, S.; Watanabe, E.; Yamada, A. Advances and issues in developing salt-concentrated battery electrolytes. *Nat. Energy* **2019**, *4*, 269–280.
- (48) Wang, A. A.; Hou, T.; Karanjavala, M.; Monroe, C. W. Shifting-reference concentration cells to refine composition-dependent transport characterization of binary lithium-ion electrolytes. *Electrochim. Acta* **2020**, 358, No. 136688.
- (49) Bergstrom, H. K. Characterizing Ion Correlation and Transport in Next-Generation Lithium Battery Electrolytes. Ph.D. Thesis, University of California, Berkeley, CA, USA, 2023.
- (50) Fong, K. D.; et al. Ion Transport and the True Transference Number in Nonaqueous Polyelectrolyte Solutions for Lithium Ion Batteries. *ACS Cent Sci.* **2019**, *5*, 1250–1260.
- (51) Kilchert, F.; et al. A volume-based description of transport in incompressible liquid electrolytes and its application to ionic liquids. *Phys. Chem. Phys.* **2023**, 25, 25965–25978.
- (52) Zhao, J.; Wang, L.; He, X.; Wan, C.; Jiang, C. Determination of Lithium-Ion Transference Numbers in LiPF6—PC Solutions Based on Electrochemical Polarization and NMR Measurements. *J. Electrochem. Soc.* 2008, 155, A292.
- (53) Capiglia, C.; et al. 7Li and 19F diffusion coefficients and thermal properties of non-aqueous electrolyte solutions for rechargeable lithium batteries. *J. Power Sources* **1999**, 81–82, 859–862.
- (54) Safa, M.; Chamaani, A.; Chawla, N.; El-Zahab, B. Polymeric Ionic Liquid Gel Electrolyte for Room Temperature Lithium Battery Applications. *Electrochim. Acta* **2016**, *213*, 587–593.
- (55) Wohde, F.; Balabajew, M.; Roling, B. Li+ Transference Numbers in Liquid Electrolytes Obtained by Very-Low-Frequency Impedance Spectroscopy at Variable Electrode Distances. *J. Electro*chem. Soc. 2016, 163, A714.
- (56) Shigenobu, K.; Dokko, K.; Watanabe, M.; Ueno, K. Solvent effects on Li ion transference number and dynamic ion correlations in glyme- and sulfolane-based molten Li salt solvates. *Phys. Chem. Chem. Phys.* **2020**, 22, 15214–15221.
- (57) Zugmann, S.; et al. Measurement of transference numbers for lithium ion electrolytes via four different methods, a comparative study. *Electrochim. Acta* **2011**, *56*, 3926–3933.
- (58) Sudoh, T.; et al. Li-Ion Transport and Solution Structure in Sulfolane-Based Localized High-Concentration Electrolytes. *J. Phys. Chem. C* **2023**, *127*, 12295–12303.
- (59) Bagheri, A.; Fazli, M.; Bakhshaei, M. Effect of temperature and composition on the surface tension and surface properties of binary mixtures containing DMSO and short chain alcohols. *J. Chem. Thermodyn* **2016**, *101*, 236–244.
- (60) Guanhua, N.; et al. Effect of NaCl-SDS compound solution on the wettability and functional groups of coal. *Fuel* **2019**, 257, No. 116077.
- (61) Wang, F.; Li, X. Effects of the Electrode Wettability on the Deep Discharge Capacity of Li-O2 Batteries. ACS Omega 2018, 3, 6006-6012.
- (62) Wang, F.; Li, X.; Hao, X.; Tan, J. Review and Recent Advances in Mass Transfer in Positive Electrodes of Aprotic Li-O2 Batteries. *ACS Appl. Energy Mater.* **2020**, *3*, 2258–2270.

- (63) Lu, Z.; et al. A rechargeable Li–CO2 battery based on the preservation of dimethyl sulfoxide. *J. Mater. Chem. A Mater.* **2022**, *10*, 13821–13828.
- (64) Dias, A. M. A.; Gonçalves, C. M. B.; Legido, J. L.; Coutinho, J. A. P.; Marrucho, I. M. Solubility of oxygen in substituted perfluorocarbons. *Fluid Phase Equilib.* **2005**, 238, 7–12.
- (65) Schürmann, A.; et al. Diffusivity and Solubility of Oxygen in Solvents for Metal/Oxygen Batteries: A Combined Theoretical and Experimental Study. *J. Electrochem. Soc.* **2018**, *165*, A3095.
- (66) Younesi, R.; Hahlin, M.; Björefors, F.; Johansson, P.; Edström, K. Li–O2 Battery Degradation by Lithium Peroxide (Li2O2): A Model Study. *Chem. Mater.* **2013**, 25, 77–84.
- (67) Li, J.; et al. Polarized nucleation and efficient decomposition of Li2O2 for Ti2C MXene cathode catalyst under a mixed surface condition in lithium-oxygen batteries. *Energy Storage Mater.* **2021**, 35, 669–678